



Aortic valve neocuspidization and bioprosthetic valves: Evaluating turbulence haemodynamics

Emily Louise Manchester ^{a,b,*}, Selene Pirola ^{a,c}, Sergio Pirola ^d, Giorgio Mastroiacovo ^d, Gianluca Polvani ^{d,e}, Gianluca Pontone ^{e,f}, Xiao Yun Xu ^a

^a Department of Chemical Engineering, Imperial College London, London, United Kingdom

^b Department of Fluids and Environment, The University of Manchester, Manchester, United Kingdom

^c Department of BioMechanical Engineering, Delft University of Technology, Delft, Netherlands

^d Department of Cardiovascular Surgery, Centro Cardiologico Monzino IRCCS, Milan, Italy

^e Department of Biomedical, Surgical and Dental Sciences, University of Milan, Milan, Italy

^f Department of Perioperative Cardiology and Cardiovascular Imaging, Centro Cardiologico Monzino IRCCS, Milan, Italy

ARTICLE INFO

Keywords:

Aortic valve neocuspidization
Aortic valve replacement
Bioprosthesis
Turbulence
Large-eddy simulation
Computational fluid dynamics
Haemodynamics
Ozaki procedure
Blood flow
Wall shear stress

ABSTRACT

Aortic valve disease is often treated with bioprosthetic valves. An alternative treatment is aortic valve neocuspidization which is a relatively new reparative procedure whereby the three aortic cusps are replaced with patient pericardium or bovine tissues. Recent research indicates that aortic blood flow is disturbed, and turbulence effects have yet to be evaluated in either bioprosthetic or aortic valve neocuspidization valve types in patient-specific settings. The aim of this study is to better understand turbulence production in the aorta and evaluate its effects on laminar and turbulent wall shear stress. Four patients with aortic valve disease were treated with either bioprosthetic valves (n=2) or aortic valve neocuspidization valvular repair (n=2). Aortic geometries were segmented from magnetic resonance images (MRI), and 4D flow MRI was used to derive physiological inlet and outlet boundary conditions. Pulsatile large-eddy simulations were performed to capture the full range of laminar, transitional and turbulence characteristics in the aorta. Turbulence was produced in all aortas with highest levels occurring during systolic deceleration. In the ascending aorta, turbulence production is attributed to a combination of valvular skew, valvular eccentricity, and ascending aortic dilation. In the proximal descending thoracic aorta, turbulence production is dependent on the type of arch-descending aorta connection (e.g., a narrowing or sharp bend) which induces flow separation. Laminar and turbulent wall shear stresses are of similar magnitude throughout late systolic deceleration and diastole, although turbulent wall shear stress magnitudes exceed laminar wall shear stresses between 27.3% and 61.1% of the cardiac cycle. This emphasises the significance of including turbulent wall shear stress to improve our comprehension of progressive arterial wall diseases. The findings of this study recommend that aortic valve treatments should prioritise minimising valvular eccentricity and skew in order to mitigate turbulence generation.

1. Introduction

Aortic valve disease (AVD) is one of the most common cardiovascular diseases worldwide and is associated with high morbidity and mortality [1]. AVD inhibits proper function of the aortic valve and is typically caused by calcification of the valve leaflets which leads to leaflet remodelling and thickening. It can cause serious complications such as sudden death or heart failure [2,3] and is linked to progressive secondary diseases including left ventricular hypertrophy [3]; arterial wall-related diseases such as dilation, aneurysm and dissection [4, 5]; aortic atherosclerosis [6] and hypertension [7] amongst others. AVD can be treated with surgical aortic valve replacement; which

is an invasive treatment involving replacement with mechanical or biological valve types. Mechanical heart valves (MHV) have superb durability although they are highly thrombogenic [8], and produce abnormal haemodynamics compared to normal aortic valves [9]. Biological (or bioprosthetic) valves (BV) typically contain treated porcine or bovine valve leaflets sewn into a stent. Biological valves can better replicate healthy aortic haemodynamics and have low thrombogenicity, although valve leaflets are prone to progressive calcification and subsequent restenosis. BV have shorter lifespans than MHV [9]. Goldstone et al. compared long-term mortality, rates of re-operation, stroke incidence and bleeding incidence between cohorts of patients who

* Corresponding author.

E-mail addresses: emily.manchester@manchester.ac.uk (E.L. Manchester), s.pirola@tudelft.nl (S. Pirola), yun.xu@imperial.ac.uk (X.Y. Xu).

underwent aortic valve replacement with MHV or BV [10]. Compared to BV, they found that MHV had long-term mortality benefit up to 55 years of age and no significant long-term mortality difference amongst patients between 55 and 64 years of age. MHV had a higher cumulative incidence of bleeding and, in some age groups, stroke, whilst BV had higher incidence of re-operation. Despite their respective advantages and disadvantages, both MHV and BV are considered gold standard in AVD treatment and each is preferred in different scenarios.

A relatively new reparative procedure has emerged, known as aortic valve neocuspidization (AV-Neo) which utilises the Ozaki procedure [11] by surgically removing diseased valve leaflets and replacing them with patient pericardium or bovine tissues. This procedure involves surgical replacement of the valve leaflets only and preserves the patient's aortic root, unlike MHV and BV replacements — hence the term repair rather than replace. The Ozaki procedure looks promising thus far based on a medium-term study which retrospectively found satisfactory outcomes in 850 patients who underwent AV-Neo following aortic valve disease diagnosis [12]. Studies into the procedure's long-term outcomes are required, and haemodynamic performance has not yet been evaluated thoroughly.

To supplement the limited clinical studies, there are a handful of studies into haemodynamic-related performance of AV-Neo. In our recent study, Pirola et al. [13] investigated valvular performance on ascending aortic wall shear stresses (WSS); a known biomarker correlated with various arterial wall diseases. 4D flow MRI was used to inform patient-specific CFD simulations of 10 patients who underwent AV-Neo and 10 patients who underwent surgical repair with biological prostheses. We found that WSS were significantly lower along the outer curvature of the ascending aorta in the AV-Neo population, compared to bioprosthetic valves. Secinaro et al. [14] performed an image-based investigation on paediatric patients who underwent AV-Neo and Ross procedures (10 of each). In this study, WSS was estimated directly from 4D flow MRI and no significant differences were found in the proximal ascending aorta between the two groups.

Blood flow in the aorta is often assumed laminar, however AVD and valve prostheses can significantly alter flow causing significant deviations from the normal aortic haemodynamics; which is already complex. This complexity combined with the pumping action of the heart creates conditions capable of producing laminar to turbulence transition, and relaminarization all within a single cardiac cycle. Emerging research indicates that blood flow is inherently disturbed [15,16] and these disturbances can have significant impact on haemodynamic metrics that are predictive of progressive arterial disease [8,17–19]. Only a few studies considered turbulence effects in AVD and valve replacements [20–23], and none with a focus on aortic valve replacements and repair in patient-specific settings. Little is known about the level of turbulence and its effects on aortic haemodynamics in both diseased and prosthetic aortic valves. Quantitative analysis of turbulence associated with prosthetic valves under patient-specific conditions could help to assess valve performance and to improve current and new treatments. In this study we will conduct turbulence-resolving, large-eddy simulations of select patient-specific aortas having undergone aortic valve replacement with bioprosthetic valves (BV) and aortic valve repair with AV-Neo. The aim of this study is to gain preliminary understanding of turbulence production in the aorta following these procedures and to quantify turbulence effects on WSS.

2. Materials and methods

2.1. Computational model

Large-eddy simulation (LES) is a numerical method capable of capturing laminar, transitional and turbulence characteristics, and has been used to model various cardiovascular flows [22–25]. Considering pulsatile aortic flows can exhibit all three states, LES is determined to

be the most suitable modelling approach. The spatially filtered Navier–Stokes equations for an incompressible fluid are given by the filtered continuity and momentum equations:

$$\frac{\partial \bar{u}_i}{\partial x_i} = 0 \quad (1)$$

$$\frac{\partial \bar{u}_i}{\partial t} + \frac{\partial}{\partial x_j} (\bar{u}_i \bar{u}_j) = -\frac{1}{\rho} \frac{\partial \bar{p}}{\partial x_i} + \nu \frac{\partial}{\partial x_j} \left(\frac{\partial \bar{u}_i}{\partial x_j} \right) - \frac{\partial \tau_{ij}}{\partial x_j} \quad (2)$$

where u is the velocity, p the pressure, ρ the density and ν the kinematic viscosity [26]. The overbar denotes spatial filtering, accounting for the resolved velocity and pressure fields. The contribution from the small, unfiltered scales are modelled by the subgrid-scale tensor, τ , whose function is to remove kinetic energy from the resolved scales, mimicking the energy cascade. The most common method in modelling the subgrid-scale (SGS) term is an eddy-viscosity approach [27]:

$$\tau_{ij} - \frac{1}{3} \tau_{kk} \delta_{ij} = -2\nu_T \bar{S}_{ij} \quad (3)$$

where $\bar{S}_{ij} = \frac{1}{2} \left(\frac{\partial \bar{u}_i}{\partial x_j} + \frac{\partial \bar{u}_j}{\partial x_i} \right)$ is the strain-rate tensor of the resolved field and ν_T represents the modelled eddy-viscosity. In this study we have selected the wall-adapting local eddy viscosity (WALE) model which has been used in a wide range of cardiovascular applications [28,29]:

$$\nu_T = (C_w \Delta)^2 D_w(u) \quad (4)$$

$C_w = 0.325$ is the constant model coefficient, Δ is the filter width which is a function of the mesh cell size and D_w is the WALE-specific operator based on invariants of the resolved velocity gradient tensor:

$$D_w = \frac{\left(S_{ij}^d S_{ij}^d \right)^{3/2}}{\left(\bar{S}_{ij} \bar{S}_{ij} \right)^{5/2} + \left(S_{ij}^d S_{ij}^d \right)^{5/4}} \quad (5)$$

S_{ij}^d is the traceless, symmetric part of the square of the resolved velocity gradient tensor:

$$S_{ij}^d = \frac{1}{2} \left(\frac{\partial \bar{u}_k}{\partial x_i} \frac{\partial \bar{u}_j}{\partial x_k} + \frac{\partial \bar{u}_k}{\partial x_j} \frac{\partial \bar{u}_i}{\partial x_k} \right) - \frac{1}{3} \delta_{ij} \frac{\partial \bar{u}_k}{\partial x_i} \frac{\partial \bar{u}_l}{\partial x_k} \quad (6)$$

Simulations were performed in OpenFOAM using the pimpleFoam solver and converged to a normalised residual of $1e-5$ at each time-step for velocity and pressure. Spatial and temporal discretisation was achieved using a second-order differencing scheme (Gauss) and a second-order implicit backwards Euler scheme, respectively. A time-step of $2e-4$ was used for all simulations, ensuring a mean CFL number less than unity throughout the cardiac cycle. Fluid properties are selected to be representative of blood with density, $\rho = 1060 \text{ kg/m}^3$ and dynamic viscosity, $\mu = 0.0035 \text{ Pa s}$. Simulations were ran on Cirrus UK National Tier-2 HPC and used 216 or 252 cores. Depending on the patient, simulations took between 7 and 14 days to simulate 24 or 25 cardiac cycles. The LES methodology was validated by the authors in an idealised medical device under transitional flow conditions [30] and was subsequently implemented and verified in patient-specific aortic flows [22,23].

2.2. Patient recruitment and selection

20 patients with aortic valve disease were recruited at Centro Cardiologico Monzino (Milan, Italy) and enrolled in our former study [13]. 10 patients underwent AV-Neo using the Ozaki technique [11] and 10 patients underwent aortic valve replacement with Carpentier-Edwards Magna biological valves. The aortic valve replacement group was chosen to closely match the 10 selected patients from the AV-Neo cohort in terms of body mass index (BMI), ejection fraction, and aortic valve pathology. In the current study we selected a subset of four patients from the total cohort; two each of AV-Neo and aortic valve repair. The baseline characteristics of the four patients are described in Table 1. The original cohort had ascending aortic diameters in both the normal

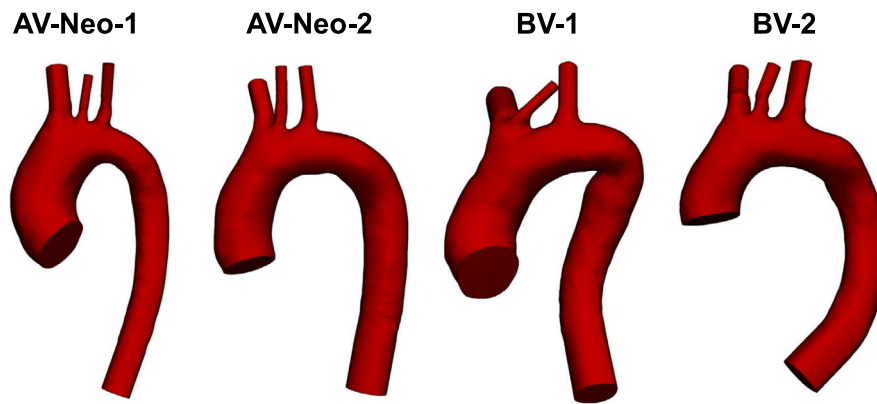


Fig. 1. Aortic surfaces segmented from MRI and trimmed at suitable branch locations.

Table 1

Patient characteristics. BMI: body mass index; BSA: body surface area.

Variable	AV-Neo-1	AV-Neo-2	BV-1	BV-2
Age [years]	27	44	71	70
Sex, [M/F]	M	M	M	M
Height [cm]	172	195	174	170
Weight [kg]	72	103	85	85
BMI [kg/m ²]	24	27	28	29
BSA [m ²]	1.8	2.4	2.0	2.0

range (< 40 mm) and mildly dilated range (40 – 45 mm) range. This is expected considering surgical intervention for the dilated ascending aorta is not typically recommended until the diameter exceeds ~ 55 mm. To evaluate turbulence haemodynamics in both scenarios, we randomly selected one normal and one dilated ascending aorta from each of AV-Neo and aortic valve repair groups. This resulted in four patients total; two AV-Neo, one with normal and one with dilated AAO; and two aortic valve repair, one with normal and one with dilated AAO. From here on, the two patients who underwent aortic valve neocuspidization are referred to as AV-Neo-1 and AV-Neo-2, and the two patients who underwent aortic valve replacement with biological valves are referred to as BV-1 and BV-2 (Fig. 1). In the current study, patients AV-Neo-1, AV-Neo-2, BV-1 and BV-2 correspond to P1, P3, P2 and P18, respectively in Pirola et al. [13]. The present study was run concurrently with the former [13] and no knowledge of the simulated haemodynamic characteristics was known prior to patient selection.

2.3. Magnetic resonance image acquisition and processing

Magnetic resonance images (MRI) were acquired using a 1.5 T system (Discovery MR 450, GE Healthcare, Waukesha, WI). MRI scans were cardiac and breath gated, and images were acquired in the standard aortic aligned axis. Aortic geometries were segmented from bright-blood MRI with uniform pixel spacings of 0.66 mm and slice thickness of 3 mm. 4D flow MRI was also acquired, which measures spatio-temporal blood flow velocities in three velocity components; anterior-posterior (AP), foot-head (FH) and right-left (RL). 4D flow MRI had uniform pixel spacings of 1.33 mm and slice thickness of 3 mm, velocity encoding (VENC) of 2 m/s in all directions, and acquisition of 30 time points per cardiac cycle. Full details on the 4D flow MRI protocol can be found in our previous publication [13]. The study design was approved by the local Ethics Committee (CCM 1373) and all patients signed the informed consent for research purposes. Aortic geometries were segmented from MRI using Materialise Mimics (v20.0, Materialise, Leuven, Belgium) and are inclusive of the ascending aorta, aortic arch, three supra-aortic branches, and descending thoracic aorta. The four segmented aortas are shown in Fig. 1.

2.4. Computational mesh

Structured computational meshes were generated using ANSYS ICEM (v17.0, ANSYS Inc., Canonsburg, Pa). Meshes consisted of 4.6–7.0 million hexahedral cells and had mean cell lengths between 0.44 and 0.51 mm. The first wall-adjacent cell heights were selected to ensure that cells lie within the viscous sub-layer, ensuring $y^+ < 1$ throughout the entire domain. Mesh sensitivity tests were conducted for each of the four aortas. Mean wall shear stress (WSS), turbulent WSS, mean kinetic energy (KE) and turbulence kinetic energy (TKE) were analysed to ensure mesh independence of both mean and turbulence related parameters. Parameters were spatially averaged over the entire simulated aortic geometry and over a selected region of interest where flow exhibits high turbulence levels. Results were considered mesh independent when differences relative to the finest mesh were less than 5%, although values were typically much smaller than this (mean relative error, 1.7%). Subgrid-scale model contributions to LES simulations were quantified by taking the ratio of modelled (TKE_{SGS}) to total (TKE_{resolved} + TKE_{SGS}) turbulence kinetic energy. Between 92.2% and 97.4% of the flow field was resolved in all aortic cases. Pope et al. [31] proposed the former as a measure of LES mesh quality and states that a value of at least 85% represents a well resolved large-eddy simulation [24,31]. Full details on mesh characteristics and mesh sensitivity results are provided in Supplementary Material.

2.5. Boundary conditions

Model inlets were placed in the ascending aorta just downstream of the sinotubular junction. For each aorta, patient-specific inlet velocity profiles were derived from 4D flow MRI. These time-dependent 3D velocity profiles are representative of the patient's aortic valvular flow. Representative inlet velocity contours at key times throughout the cardiac cycles are shown in Fig. 2 for each aorta. At all branch and descending thoracic aorta outlets, a three-element Windkessel model was imposed. Windkessel parameters were calculated using derived flow rates and mean arterial pressure which was assumed to be 100 mmHg as central pressure measurements were unavailable for this cohort. Calculated parameters for proximal resistance, distal resistance and arterial compliance used for each aorta are provided in Supplementary Material. Vessel walls were assumed rigid with a no-slip boundary condition.

2.6. Post-processing disturbed pulsatile flows

In disturbed pulsatile flows, cycle-to-cycle variations occur. An instantaneous variable, ϕ , can be decomposed into phase-averaged and fluctuating components using a Reynolds like decomposition:

$$\phi(\mathbf{x}, t) = \langle \phi \rangle(\mathbf{x}, t) + \phi'(\mathbf{x}, t) \quad (7)$$

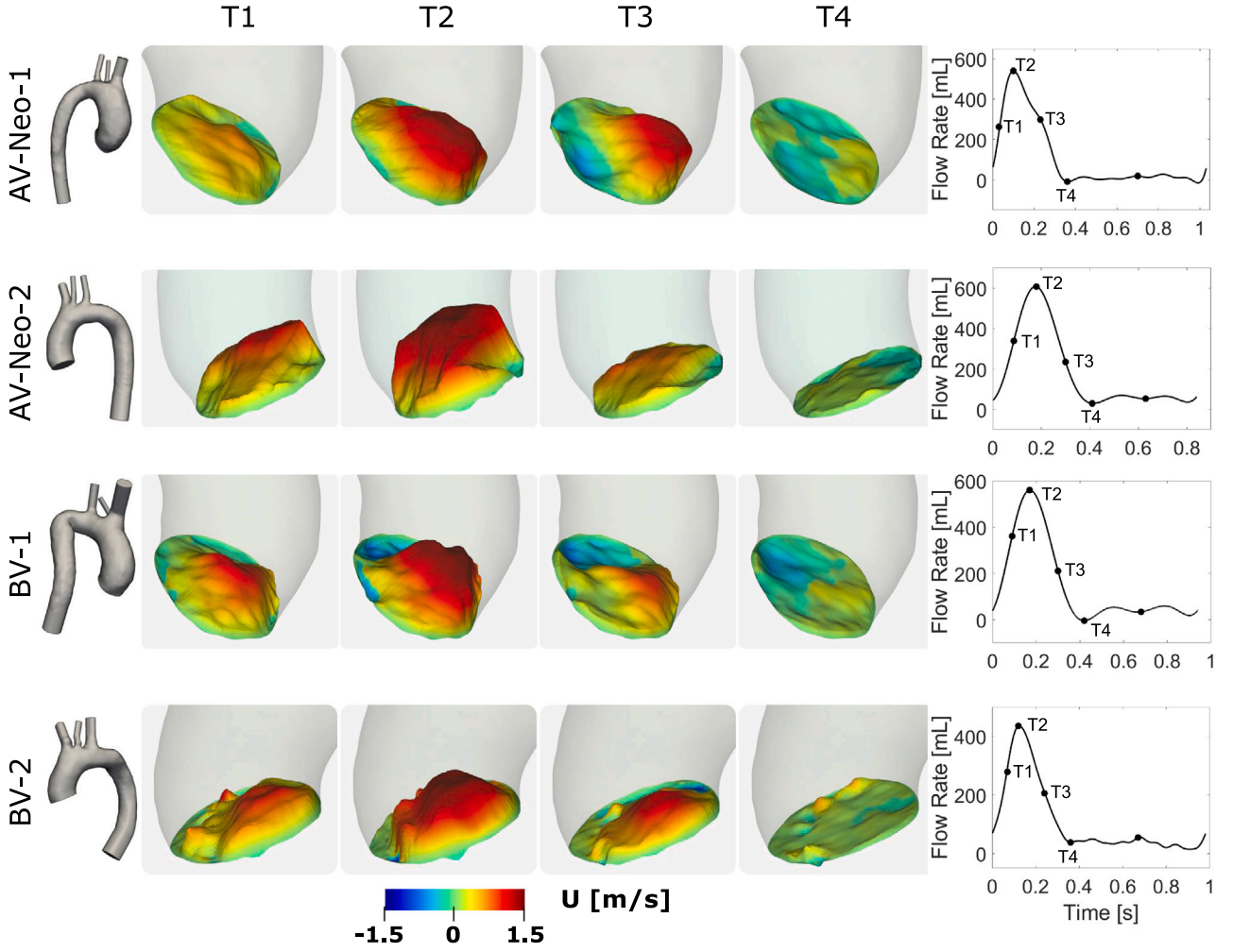


Fig. 2. A selection of the inlet 3D velocity contours at four key times throughout the cardiac cycle, and inlet flow waveforms.

When multiple cardiac cycles are simulated the phase-average operator, $\langle \cdot \rangle$ represents the mean value of a variable at a specified time within a cardiac cycle, e.g., peak systole.

$$\langle \phi \rangle(\mathbf{x}, t) = \frac{1}{N} \sum_{n=0}^{N-1} \phi(\mathbf{x}, t + nT) \quad (8)$$

N is the total number of cardiac cycles, T the period of the cardiac cycle and t is a specified time within a cycle. For disturbed pulsatile flows, the phase-average provides the correct mean representation of a variable at any given time in the cardiac cycle. The phase-averaged fluctuating component is defined as the root-mean-square (RMS) of the instantaneous and phase-average variables:

$$\langle \phi' \rangle(\mathbf{x}, t) = \sqrt{\frac{1}{N} \sum_{n=0}^{N-1} (\phi(\mathbf{x}, t + nT) - \langle \phi \rangle(\mathbf{x}, t))^2} \quad (9)$$

Integrating any variable over the full cardiac cycle results in a cycle-average, referred to as the time-average. This can be calculated for both mean and fluctuating variables, giving the time-averaged mean variable:

$$\overline{\langle \phi \rangle}(\mathbf{x}, t) = \frac{1}{T} \int_0^T \langle \phi \rangle(\mathbf{x}, t) dt \quad (10)$$

and the time-averaged turbulent variable:

$$\overline{\langle \phi' \rangle}(\mathbf{x}, t) = \frac{1}{T} \int_0^T \langle \phi' \rangle(\mathbf{x}, t) dt \quad (11)$$

The treatment described in this section can be applied to any variable in pulsatile flows and will form the post-processing basis of this paper. For example, applying Eqs. (8)–(9) to the wall shear stress (WSS) gives the phase-averaged (mean) WSS and phase-averaged turbulent WSS at a given time in the cardiac cycle. Applying Eqs. (10)–(11) to the WSS gives the time-averaged mean WSS and time-averaged turbulent WSS. In this study we will present phase-averaged: velocity, turbulence kinetic energy and wall shear stress. Depending on the aorta, 24 or 25 cardiac cycles were simulated in total, with the first cycle neglected to remove initialisation effects. Phase-averaging of all mean and fluctuating parameters was subsequently performed on all 23 or 24 simulated cardiac cycles. The phase-averaged parameters were considered converged when errors relative to the final cycle were less than 2%. Cumulative phase-averaged plots of KE, TKE, laminar WSS and turbulent WSS for all aortas are provided in Supplementary Material.

3. Results

3.1. Comparison with 4D flow MRI

Aortic velocity fields measured with 4D flow MRI and those obtained with LES are quantitatively compared using Pearson's product-moment correlation coefficient, R . This statistical method gives a normalised measure of the covariance of two variables, quantifying the linearity between two data-sets [32]. $R \in [0, 1]$ where $R = 0$ indicates

Table 2

Pearson correlation coefficients, R_i , for each of the three components of velocity, calculated using the entire aortic fluid domain. R_i is calculated using phase-averaged velocities, $\langle u_i \rangle$.

Valve Type	Time	R_1	R_2	R_3
AV-Neo-1		0.89	0.94	0.83
AV-Neo-2	Peak	0.86	0.91	0.66
BV-1	Systole	0.78	0.85	0.73
BV-2		0.84	0.88	0.81
AV-Neo-1		0.77	0.88	0.67
AV-Neo-2	Mid-Systolic	0.75	0.84	0.64
BV-1	Deceleration	0.56	0.66	0.59
BV-2		0.57	0.63	0.57

negligible correlation and $R = 1$ indicates perfect correlation between the variables. Pearson's correlation coefficient is calculated for each phase-averaged velocity component, over the entire aortic CFD domain at peak systole, providing a point-by-point comparison throughout the velocity field. Velocity fields from all LES simulations are spatially down-sampled to match 4D flow MRI spatial resolution, as recommended in [33]. In cardiovascular flows, largest differences between 4D flow MRI and CFD velocity fields are typically observed at peak systole [33,34], motivating comparison at this time. Comparisons are also made at mid-systolic deceleration when flow is in a chaotic state and peak turbulence levels are typically observed. These time points represent distinct challenges for the LES simulation. Large-scale flow features associated with laminar flow occur at peak systole and small-scale flow features associated with turbulence occur at mid-systolic deceleration. Values for Pearson correlation coefficients are given in Table 2 and correlation plots for the velocity components are provided in Supplementary Material. $R > 0.7$ indicate a high positive correlation and $R > 0.5$ indicate a moderate positive correlation [32]. For each of the three velocity components, all LES simulations show a high positive correlation with 4D flow MRI velocities at peak systole, except AV-Neo-2 which shows a high positive correlation in the x and y -components of velocity and a moderate positive correlation in the z -component of velocity. At mid-systolic deceleration, a high positive correlation is seen in both AV-Neo patients. Both BV patients show a high positive correlation in the y -component of velocity and a moderate positive correlation in the x and z -component of velocity. Qualitative comparisons are also made through comparison of velocity streamlines throughout the aorta at peak systole and mid-systolic deceleration (see Supplementary Material). Overall, the LES simulations are able to accurately capture primary and secondary flow features including jet skew, recirculation, counter-rotating vortices and helical flow. Detailed analysis of each patient is provided in Supplementary Material. These findings indicate that aortic velocity fields are accurately reproduced by our LES simulations.

3.2. Anatomical and physiological features

In this patient cohort we observed differing valvular performance and subsequent varying haemodynamics in the ascending aorta. To better evaluate turbulence production we first highlight anatomical and physiological differences amongst the cohort. Aortic diameters were measured at various intrathoracic levels from MR images (Fig. 3) and compared with measurements from a previous study of healthy aortas ($n=70$) [35]. The intrathoracic levels measured in [35] correspond to levels at the aortic valve sinus; ascending aorta (AAo) at its maximum diameter; the aortic isthmus which is the segment of the aorta located just distal to the left subclavian artery; the proximal descending aorta (DAo); and the distal DAo. In this study, MR image segmentations did not include the aortic valve sinus because computational inlets were placed just after the sinotubular junction, therefore computational model inlet diameters are also included in Fig. 3. Data from [35] plotted in Fig. 3 represent mean diameters [mm] averaged from 70 healthy

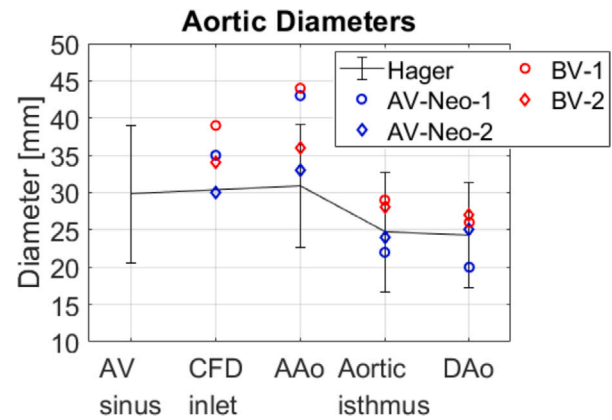


Fig. 3. Characteristic aortic diameters measured at various intrathoracic levels and compared to data published in [35]. (AV = aortic valve, AAo = ascending aorta, DAo = descending aorta).

aortas ± 2 standard deviations. The maximum AAo diameters of AV-Neo-1 and BV-1 lie outside the normal range (43 mm and 44 mm, respectively). This is indicative of AAo dilation and potential aneurysm. All other measurements are within normal ranges.

Aortic valvular skewed flow is visualised in Fig. 4 at peak systole (A) and systolic deceleration (B). The left columns of sub-figures A and B show normalised directional velocity contours at the inlet, where yellow markers indicate the point of maximum velocity. The aortic aligned reference frame is also shown overlaying the velocity contours; indicating anterior (A), posterior (P), right (R) and left (L) directions. Skew is also visualised using velocity streamlines in the ascending aorta (right column of sub-figures A and B). BV-1 exhibits the most extreme skew of all patients. Valvular flow is skewed towards the anterior wall as can be seen at both peak systole and during valve closure. This is also shown by the inlet contour plots where the bulk of valvular flow, including maximum velocity, lie in the anterior quadrants with some reversed flow in the posterior quadrants. BV-2 shows slight skew towards the right wall as can be seen by the front view of velocity streamlines at peak systole. In BV-2, the bulk of valvular flow is located in the posterior-left quadrant. Both AV-Neo valve types do not exhibit notable skew, and valvular flow is mostly central in the ascending aorta. The bulk valvular flow of AV-Neo-1 is relatively uniform at peak systole but redistributes to the anterior-left quadrant during valve closure. In AV-Neo-2, the bulk of valvular flow is the most uniformly distributed of all the patients in this study, with peak velocity occurring near the centre.

3.3. Turbulence kinetic energy

Turbulence kinetic energy (TKE) is associated with eddies in disturbed flows and is a measure of the turbulent energy in a fluid. TKE is commonly used to evaluate turbulence effects in cardiovascular flows [25,28,36,37]. Fig. 5A shows volume renderings of TKE for each aorta at four key-times throughout the cardiac cycles. To quantitatively evaluate and compare turbulence magnitudes, TKE is spatially averaged over the whole aorta and averaged over four localised regions of interest including the AAo, aortic arch, proximal-DAo and distal-DAo. This provides temporal variations of mean regional values throughout the cardiac cycle, which are plotted in Fig. 5B for each aorta alongside the corresponding flow rate. Note the different scales between aortas. An animation of TKE over the entire cardiac cycle for each aorta is shown in Video 1.

Spatially averaged TKE behaviours show similar general trends over a cardiac cycle in all four aortas. TKE is small throughout early systole in all regions and does not typically start to increase until peak systole or early deceleration. Throughout systolic decelerations there are large

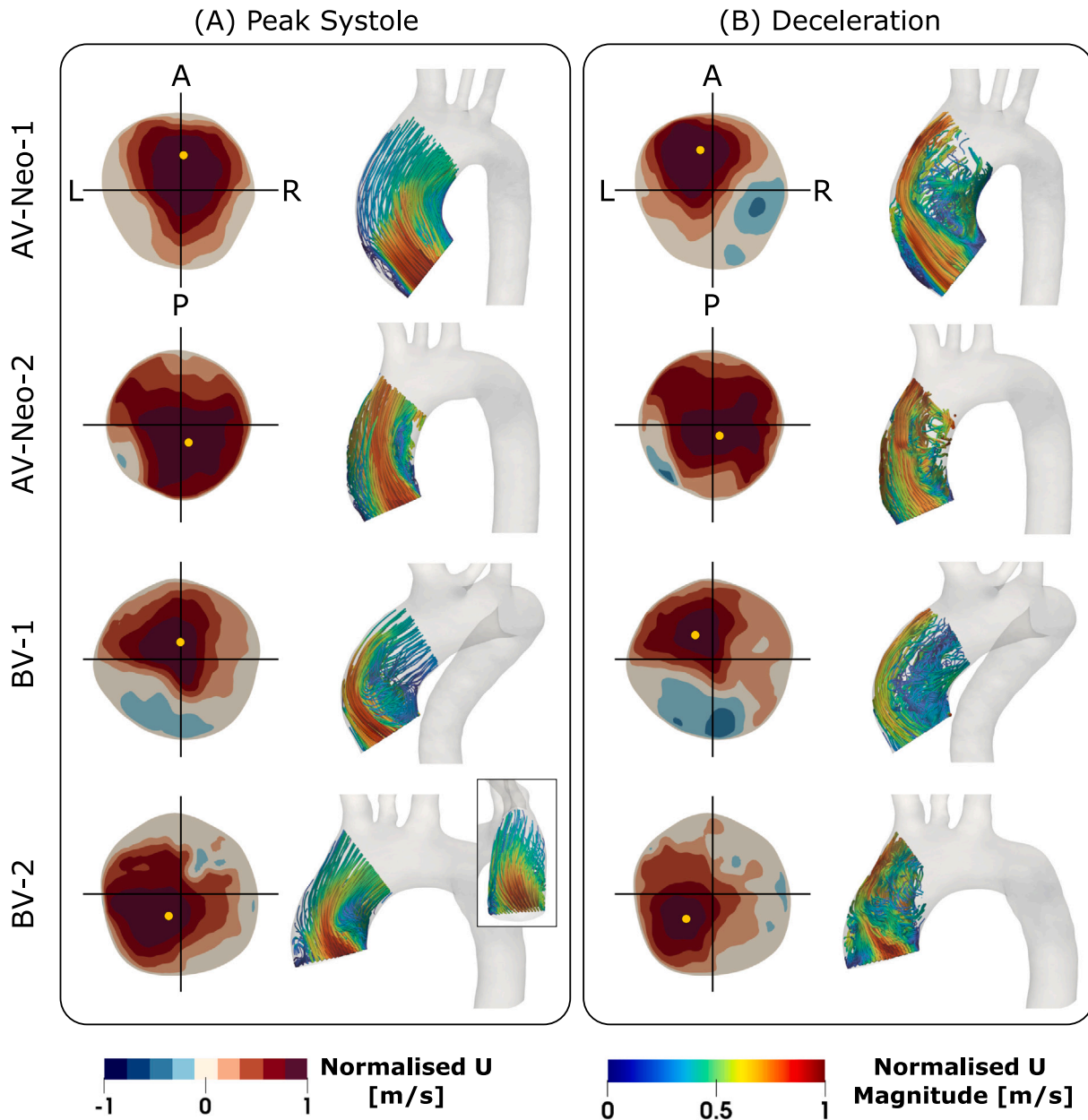


Fig. 4. Visualisation of valvular flows at (A) peak systole and (B) mid-systolic deceleration. The left sub-figures show valvular jet eccentricity at the inlet plane and the right sub-figures show skew in the ascending aorta. The yellow marker represents the point of maximum velocity. The aortic aligned reference frame overlaying the inlet velocity contours are indicated by anterior (A), posterior (P), right (R) and left (L) directions.

variations in TKE values between the aortas and different regions. Peak TKE levels occur throughout this period for all valve types. During diastole, turbulence dissipates to small levels in all aortas. TKE levels are low during diastole and early systole. Turbulence levels differ significantly among the four aortas. Considering TKE spatially averaged over the entire aorta, BV-1 shows the highest mean TKE of all aortas, peaking at 26 Pa. This is followed by AV-Neo-1 (19 Pa), BV-2 (14 Pa) and AV-Neo-2 (12 Pa). Fig. 6 compares peak values of spatially averaged TKE in different regions of interest for all four aortas. Highest peak values are typically seen in the AAo and arch (regions 1 and 2), followed by proximal-DAo and distal-DAo (regions 3 and 4), respectively.

3.4. Wall shear stress

WSS is decomposed into phase-averaged laminar and phase-averaged fluctuating components using Eqs. (8)–(9) to evaluate the mean

shear force exerted on the wall, as well as the contribution from near wall disturbances. Integrating phase-averaged wall shear stresses over the cardiac cycle gives time-averaged wall shear stress (TAWSS) (Eqs. (10)–(11)). Fig. 7A shows contours of laminar TAWSS and turbulent TAWSS for each aorta, note the different scales for laminar and turbulent TAWSS. In all valve types, laminar TAWSS is typically elevated in the AAo and some aortas show elevations on the inner arterial wall at the connection between the arch and the proximal-DAo. The locations of elevated turbulent WSS correspond to regions where wall disturbances are present. Phase-averaged laminar WSS, turbulent WSS and total WSS are spatially averaged over the entire aorta and the four regions of interest, providing mean values at each time point throughout the cardiac cycle. These spatially averaged values are plotted over a cardiac cycle in Fig. 7B. Laminar WSS shows similar trends over the cardiac cycle for all aortas and typically follows the shape

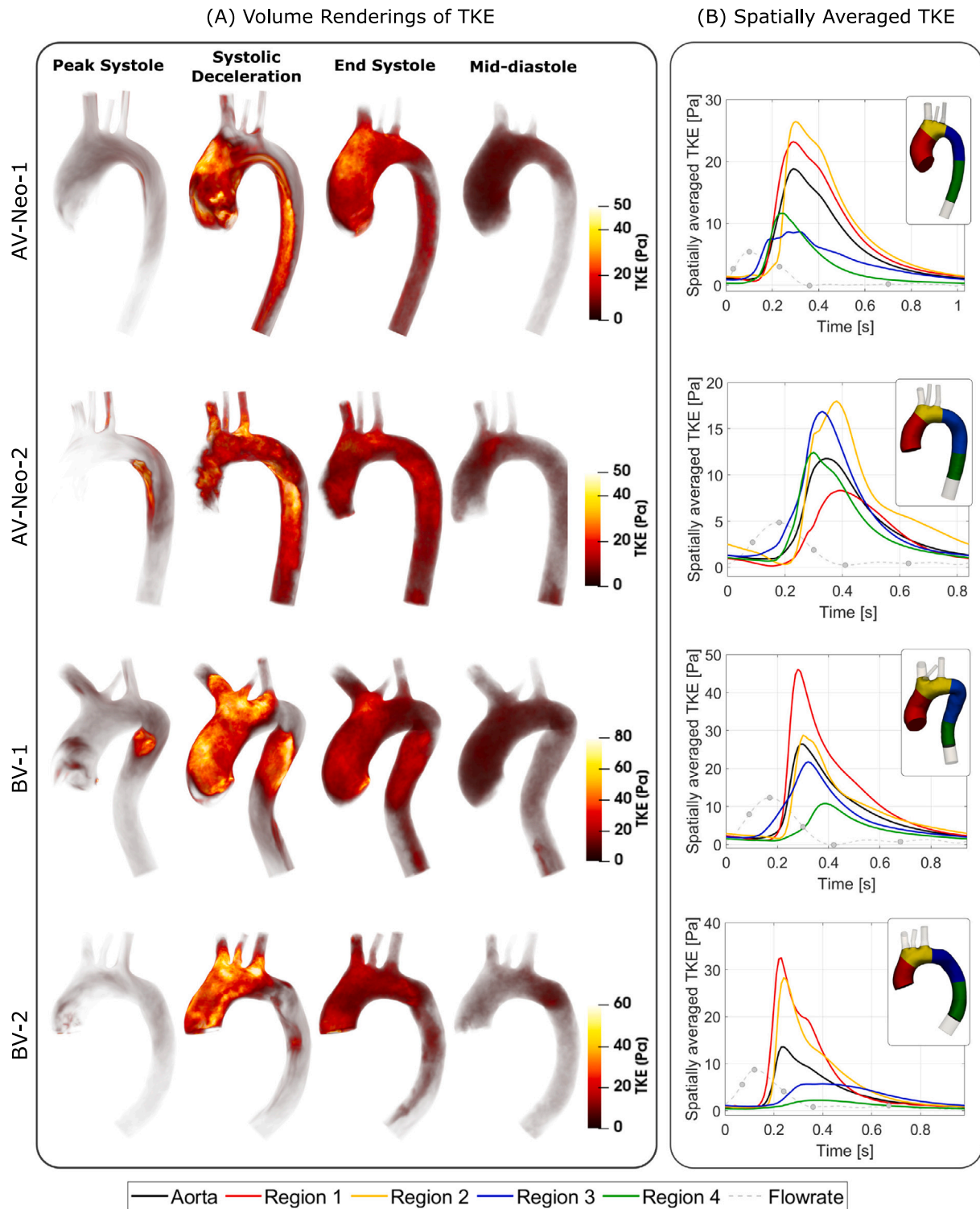


Fig. 5. Turbulence kinetic energies. (A) Volume renderings of TKE at four key times throughout the cardiac cycle. (B) TKE spatially averaged over the whole aorta and each ROI. Regions 1–4 correspond to the ascending aorta, aortic arch, proximal descending aorta and distal descending aorta. Note the different TKE scales for each aorta.

profile of inlet flow rate. Turbulent WSS also behaves in a similar manner among the aortas, which is small throughout systolic acceleration and typically increases during systolic deceleration, peaking around mid-systolic deceleration and decreasing steadily throughout diastole. Adding laminar and turbulent WSS together gives the total WSS, which represents the total shearing force experienced due to primary and fluctuating near wall velocities. The contribution from turbulent WSS during systolic acceleration is almost negligible. Between peak systole

and early systolic deceleration, peak values of total WSS occur. Considering WSS spatially averaged over the entire aorta, both AV-Neo valve types have the highest total wall shear stresses of 6.3 Pa (AV-Neo-2) and 6.8 Pa (AV-Neo-1) (Fig. 7B). The BV's have smaller peak total WSS's of 5.9 Pa (BV-1) and 4.6 Pa (BV-2). Maximum values of turbulent WSS occur around mid-systolic deceleration in all aortas. Turbulent WSS is highest in BV-1 reaching 2.3 Pa, followed by BV-2 and AV-Neo-1 (both 1.7 Pa) and AV-Neo-2 (1.4 Pa). At these times, the contribution from

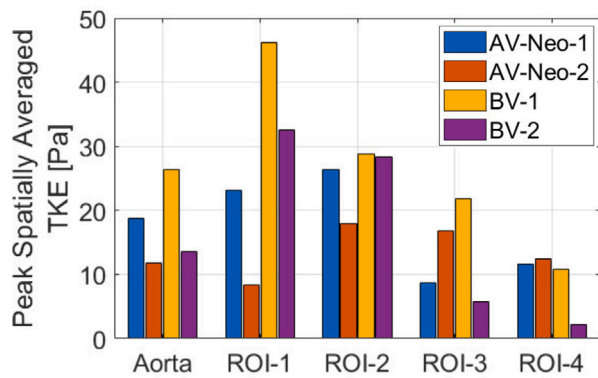


Fig. 6. Peak TKE spatially averaged over the aorta and different regions of interest (ROI-1 to ROI-4) corresponding to the AAO, aortic arch, proximal-DAo and distal-DAo, respectively.

turbulent WSS to total WSS ranges between 33.0% and 41.6%. Fig. 7B also shows that turbulent WSS is of comparable magnitudes to laminar WSS throughout late systolic deceleration and diastole. In the biological valves, turbulent WSS marginally exceeds laminar WSS for 61.1% (BV-1) and 27.3% (BV-2) of the cardiac cycle. In AV-Neo valve types, turbulent WSS marginally exceeds laminar WSS for 34.3% (AV-Neo-1) and 33.0% (AV-Neo-2) of the cardiac cycle. Turbulent WSS generally has the largest impact on total WSS during systolic deceleration and diastole.

Fig. 8 shows total TAWSS spatially averaged over the entire aorta (A) and the ascending aorta (B), broken down into laminar and turbulent TAWSS components. Over the whole aorta, spatially averaged total TAWSS ranges between 1.7 Pa (BV-2) and 2.7 Pa (AV-Neo-2). Turbulent TAWSS contributions to total TAWSS vary between 22.9% (AV-Neo-2) and 35.9% (BV-1). Considering only the AAO (Fig. 8B), spatially averaged total TAWSS ranges between 2.3 Pa (AV-Neo-1) and 3.1 Pa (BV-1). Turbulent TAWSS contributions to total TAWSS vary between 15.3% (AV-Neo-2) and 38.9% (AV-Neo-1). Even in aortas with relatively small turbulence levels, turbulent TAWSS contributes significant amounts to total TAWSS.

4. Discussion

4.1. Practical implications of turbulence

Turbulence in blood flow can significantly impact aortic haemodynamics, and parameters associated with turbulence are indicative of progressive arterial disease [8,17–19]. Endothelial cells line the inner vessel wall and their role is to regulate exchanges between the bloodstream and surrounding tissues via signalling mechanisms. Endothelial cells are highly adaptable; capable of increasing their numbers and orientation, enabling vessel remodelling via tissue growth and repair [38]. Their signal mechanisms which organise arterial remodelling are sensitive to physical forces including wall shear stress. Fluctuating WSS associated with turbulence is known to induce endothelial dysfunction and turnover [39,40]. Turbulence also contributes to risk of thrombosis through two distinct mechanisms involving endothelial cell dysfunction and the induction of localised regions of stasis. Turbulent shear stresses acting within the fluid cause mechanical blood trauma and can increase levels of haemolysis [41]. The effects of turbulence on the cardiovascular system are complex and turbulence is associated with the pathogenesis of various cardiovascular diseases. Improved comprehension of turbulence production and turbulence magnitudes in existing aortic valve bioprostheses and repair procedures will enable better device design and provide valuable insights for surgical decision-making.

4.2. Turbulence production

Turbulence characteristics differ with each aorta and are first discussed individually, starting with BV-1 which shows the highest overall turbulence levels.

BV-1: Turbulence production is attributed to both the aortic valve and the tortuous DAo, which has a sharp bend at the arch-DAo connection. BV-1 produces a skewed valvular jet which impinges on the AAO anterior wall, resulting in localised recirculation behind the jet. Furthermore, the AAO is dilated (44 mm, Fig. 3) which further exacerbates turbulence production. The sharp bend in the tortuous arch-DAo is responsible for turbulence production in the proximal-DAo region. The sharp bend affects flow such that during systolic acceleration blood flow detaches from the inner arterial wall, resulting in recirculation in the proximal DAo. Flow unsteadiness is amplified during valve closure, resulting in localised turbulence in region 3, as can be seen in Fig. 5 at systolic deceleration.

BV-2: Turbulence is produced primarily in the AAO from the aortic valve. The bulk of valvular flow is non-central, located in the posterior-left quadrant and jet flow skews slightly towards the right (Fig. 4). Because of this, the jet does not fill the entire aortic diameter which leads to disturbances and turbulence, even though the AAO diameter lies within the normal range. Similarly to BV-1, the process of valve closure increases the unsteadiness of the flow, amplifying turbulence effects (Fig. 5). At the arch-DAo connection some flow detaches and a helical region is observed during systolic deceleration, allowing some turbulence to develop although these levels are small.

AV-Neo-1: In AV-Neo-1, turbulence is mostly produced in the AAO and its production is similar to BV-1, albeit to a lesser degree. Although valvular flow is not skewed (Fig. 4), the dilated AAO (43 mm, Fig. 3) causes an effective region of expansion between the valve and AAO. This has a destabilising effect on the valvular flow, providing space for turbulence to develop. This destabilising effect is increased during valve closure. Turbulence is also produced in the arch-DAo, where some flow separates and vertical helical flow is observed.

AV-Neo-2: Turbulence production is primarily attributed to the small notch in the arch-DAo connection. Even this small notch is capable of causing separation from the inner arterial wall, resulting in a small but not insignificant region of disturbed flow (Fig. 5A at peak systole). This detachment prompts a region of vertical helical flow near the inner arterial wall. Some turbulence is also produced in the AAO and this is amplified during valve closure.

Despite differences in turbulence characteristics, all aortas show some levels of flow disturbance regardless of valve function, skew, degree of AAO dilation, etc. Recent studies also indicate that turbulence is present in the healthy adult aorta [15,16,36]. In all aortas and regions, peak TKE values occur sometime between systolic acceleration and end systole, as has been observed in other studies [28,36]. Turbulence dissipates to small amounts, but not completely, throughout the diastolic phase owing to the kinetic energy cascade. A lack of energy entering the system combined with low kinetic energies in the mean flow mean that higher levels of turbulence cannot be sustained.

In the aortas considered, turbulence is produced in; (1) the ascending aorta; and/or (2) the proximal descending thoracic aorta. Turbulence produced in the AAO is dependent on both aortic anatomy (i.e., ascending aorta dilation) and valve physiology (i.e., aortic valve function). Ha et al. [15] found that an age-related increase in AAO diameter was correlated with increased turbulence levels in the ascending aorta. In the present study, aortas with dilated ascending aortas (BV-1, AV-Neo-1) also show elevated TKE levels in the ascending aorta and arch regions (Fig. 5). In our previous study, we evaluated turbulence behaviours in a patient-specific aorta with severe aortic valve stenosis and a dilated ascending aorta [22]. We found significantly elevated turbulence levels in the AAO with spatially averaged TKE reaching 62 Pa whereas values in this region in the present study are within 9–4 Pa. In another study, various normal and stenotic mechanical and

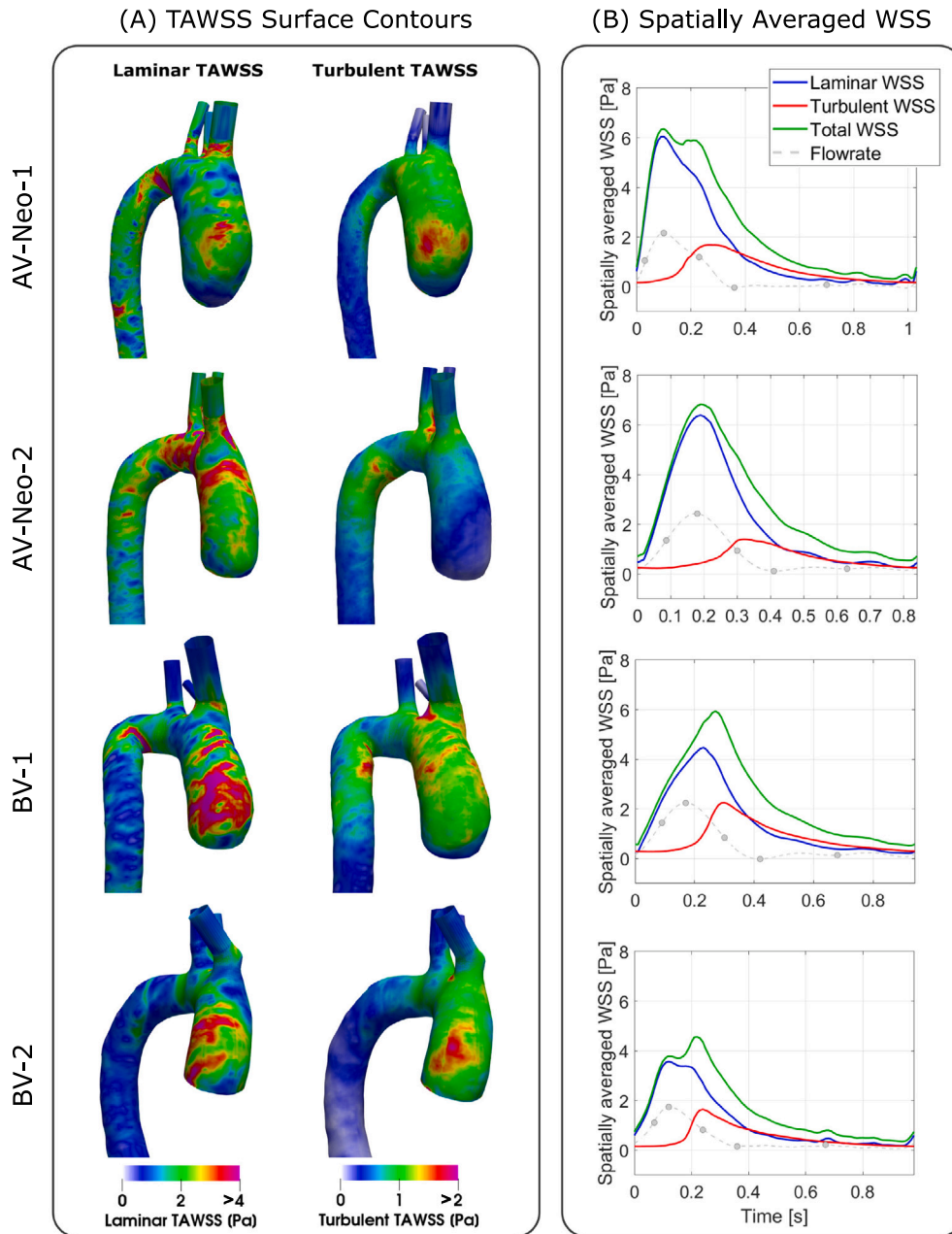


Fig. 7. Wall shear stresses. (A) Phase-averaged laminar TAWSS (left) and turbulent TAWSS (right) surface contours. (B) Laminar, turbulent and total WSS spatially averaged over the entire aorta, plotted over the cardiac cycle.

transcatheter aortic valve replacements were implanted in an idealised straight flow phantom, and flow characteristics were evaluated from MRI [42]. TKE was higher in all stenosed valve replacements, compared to their respective non-stenosed counterparts. For the biological valves in this study, both show some degree of skewed valvular flow and non-central jets. These cases have elevated TKE levels in the AAO (BV-1: 46 Pa, BV-2: 32 Pa) and are higher than TKE levels in both AV-Neo cases which show healthier valvular flow and no skew (AV-Neo-1: 23 Pa, AV-Neo-2: 9 Pa). In the proximal DAo, the degree of turbulence production is dependent on the anatomy of the arch-DAo branch connection; such as narrowing or a sharp bend. All four aortas show some helical flow in this region, regardless of local anatomical features. In aortas where significant separation from the inner descending aortic wall is observed (BV-1, AV-Neo-2), turbulence production is highest, regardless of valve function (Fig. 6). A previous study which evaluated turbulence levels

in a patient-specific aortic coarctation found elevated turbulence levels in similar regions [28].

4.3. Evaluating turbulent WSS

Valvular flows can skew towards the anterior vessel wall, meaning high near wall velocities occur in these regions. This is seen most prominently in BV-1 where the valve produces a highly skewed and eccentric valvular jet which impacts on the anterior vessel wall as discussed in Section 3.2. Turbulent wall shear stresses occur wherever near wall disturbances are present. In BV-1 for example, high TKE levels are observed in the AAO and the proximal DAo; both regions correspond to high turbulent TAWSS values (Fig. 7A). Consequently, turbulent TAWSS is elevated in the AAO of most aortas, except AV-Neo-2. The aortas which experienced flow separation and subsequent

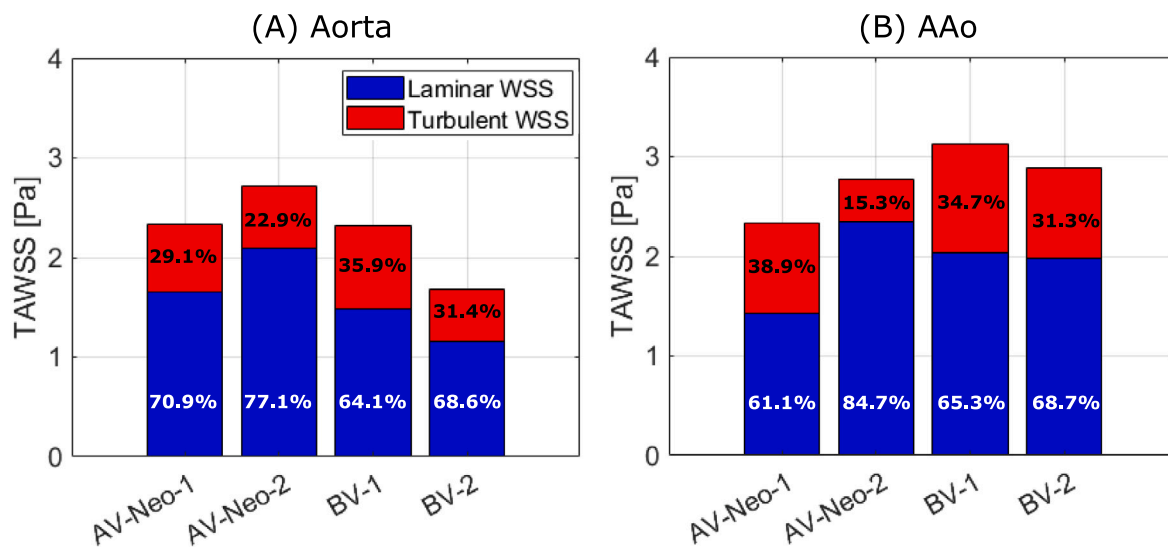


Fig. 8. Laminar TAWSS and turbulent TAWSS spatially averaged over (A) the entire aorta and (B) the ascending aorta. Percentages show laminar and turbulent contributions to total TAWSS.

disturbance in the proximal DAo (BV-1 and AV-Neo-2) also show higher turbulent TAWSS in these regions. A study into flow characteristics in a healthy aorta found similar trends to this study [43]. A recirculation zone was also observed in the proximal DAo, and elevated turbulent WSS values were observed at a point along the inner curvature in this region. Andersson et al. [29] conducted LES of an aortic coarctation pre- and post-intervention. Although aortic coarctation has not been considered in this study, it produces similar flow characteristics in the proximal DAo (separation and recirculation) but to a greater extent. The authors examined laminar and turbulent TAWSS in this region and their results showed comparable magnitudes to this study. TKE analysis showed that turbulence is highest during systolic deceleration, therefore it is not surprising that turbulent contributions to total WSS are consistently high at this time, regardless of valve type or magnitude of turbulence. Lantz et al. [43] conducted LES of a healthy adult aorta and also found that point-wise turbulent WSS could exceed laminar WSS during part of systole.

4.3.1. Clinical implications of WSS

Endothelial cells play an important role in regulating biological functions of the arterial wall. WSS has been identified as one of the factors affecting endothelial cell response, which itself plays a key role in promoting vascular remodelling and pathologies [18,19]. Specifically, high shear stresses are associated with aortic growth, extracellular matrix dysregulation and elastic fibre degeneration [8,17,44], which correlate with impaired tissue biomechanics. Soulat et al. [45] conducted an image-based longitudinal study of patients with bicuspid aortic valve. They found that areas of elevated AAo WSS were associated with higher rates of AAo dilation. Endothelial cell response is also sensitive to space-time fluctuations of WSS that occur in disturbed flows and fluctuating WSS is known to induce endothelial dysfunction [39,40]. There is abundant research linking abnormal WSS with arterial disease pathogenesis and progression [18,46]. WSS has also been used as a biomarker for the detection and evaluation of disease progression. New surgical techniques for aortic valve diseases should aim to maintain endothelial homeostasis in the aorta and, consequently, maintain WSS within a range which supports endothelial equilibrium.

Neglecting turbulence effects can result in significant underestimations of total WSS, especially throughout systolic deceleration and diastole. Regardless of valve type and turbulence magnitudes, turbulent WSS exceeded laminar WSS for significant portions of the cardiac cycle, meaning total WSS could be underestimated by at least 50% during these times if turbulence effects are neglected. Although this study

is limited to four aortas, results indicate that near wall disturbances should be included in the evaluation of TAWSS, regardless of valve type or expected turbulence levels.

4.4. Comparing AV-Neo and BV

4.4.1. Turbulence production

Stented and stentless BV's can produce an eccentric jet directed towards the anterior-right aortic wall [14], which we also observed in both BV's included in the present study. Isolating the different valve types and comparing TKE levels in the AAo shows that BV-1 with a skewed, eccentric jet and a dilated AAo has higher TKE levels than BV-2 which has a slightly skewed and mildly eccentric jet and has an AAo diameter within the healthy range. Similarly, AV-Neo-1 with a dilated AAo and mildly eccentric jet has higher TKE levels than AV-Neo-2 which has a central jet and AAo diameter within the healthy range. This can be seen by comparing peak spatially averaged TKE levels in the AAo (Fig. 6, ROI-1). Overall, turbulence levels in the AAo of the two bioprosthetic valves was greater than the two patients who underwent AV-Neo.

Turbulence production and sustainment are dependent on a large number of variables. Based on the observations in this and other studies [15,22,29], turbulence production is likely dependent on a combination of physiological and anatomical properties such as flow rate; aortic valve function including eccentricity and skew; AAo dilation; type of arch-DAo branch connection and tortuosity. AAo dilation provides sufficient space for turbulence features to develop and has been observed in both this study and another into healthy aortas [15]. Further anatomical features including arch-DAo connection and tortuosity, similar to aortic coarctation, promote flow separation from the inner arterial wall in the proximal DAo. TKE levels in the proximal DAo are linked with bigger regions of flow detachment. During systolic deceleration reduced flow enters the aorta, which has a destabilising effect on the flow field and peak TKE values occur in all aortas in this study. At this stage we cannot isolate turbulence production from each variable, and more aortas would need to be included to determine statistical correlations and quantifiably evaluate dominant mechanisms of turbulence production. From the limited cases in this study, the aorta (BV-1) with the most eccentric and skewed jet, combined with a dilated AAo has the highest turbulence levels in the AAo. BV-2 with a skewed jet and normal AAo diameter has higher turbulence levels than AV-Neo-1 with no skew but a dilated AAo. This may indicate that valvular skew may be dominant over AAo dilation in terms of turbulence production,

however this would need to be investigated with a larger sample size to confirm our hypothesis. AV-Neo-2 with healthy valvular flow and a normal AAO diameter has significantly smaller turbulence levels in the AAO compared to all other aortas.

4.4.2. Wall shear stress

In a recently published study, we investigated the impact of valvular intervention on time-averaged WSS in the ascending aorta of 20 patients with aortic valve diseases. The cohort was divided equally between individuals undergoing AV-Neo repair and those receiving BV replacements [13]. Analysis of a larger cohort was facilitated by utilising a lower-fidelity CFD modelling approach, which did not resolve turbulence. This simulation approach requires significantly less computational power as it allows for coarser spatial and temporal resolutions, and fewer cardiac cycles compared to the high-fidelity simulations used in this study. The study of 20 patients found a statistically significant reduction in time-averaged WSS along the outer curvature of the ascending aorta in the AV-Neo group compared to the BV group [13]. The authors hypothesised that the long leaflets in AV-Neo might help maintain central post-valvular flow, thereby reducing ascending aortic WSS. The present study shows that the total TAWSS – which accounts for both mean and turbulent WSS – is lower in the AAO in both AV-Neo valve types than bioprosthetic valves.

4.5. Limitations and recommendations

Whilst this study sheds light into general turbulence behaviours, the limited sample size means that statistical conclusions cannot be drawn. The cohort size was determined by a number of factors including the availability and access to high performance computing systems; data management including uploading, downloading, storing and backing up terabytes of data; and the challenging requirements of LES which require significant time dedicated to pre- and post-processing. One of the main limitations of LES are the high user and computational demands. Each main simulation took between 7 and 14 days on Cirrus UK National Tier-2 HPC Service, utilising 216 or 252 cores. It is estimated that the turnaround time from acquiring imaging data to generating post-processed results for one aortic case took around 1.5 to 2 months, including both user and computational time. Reducing these demands would allow more physiologically accurate simulation, faster simulation, and/or a greater number of simulations to be conducted. Future studies should increase sample size for proper statistical analysis and include other gold standard treatments for aortic valve disease including mechanical heart valves and transcatheter aortic valve replacement.

5. Conclusion

This study explored turbulence production and its effects on wall shear stress in aortas with bioprosthetic and aortic valve neocuspidization valve types. We performed LES simulations of four patient-specific aortas and verified simulation velocity fields through comparison with 4D flow MRI. Good correlations were achieved in all cases. Our LES simulations showed that turbulence was present in all aortas and was small during systolic acceleration, peaking during systolic deceleration and dissipating to low levels throughout diastole, although not diminishing completely. Regional analysis of TKE was performed to better understand behaviours and it was found that turbulence was produced in the ascending aorta and/or the proximal descending thoracic aorta. Turbulence produced in the ascending aorta was dependent on both local anatomical features and valve physiology (e.g., AAO dilation, valve eccentricity and skew). Proximal descending thoracic aorta disturbances were dependent on anatomy of the arch-DAo connection (e.g., narrowing or a sharp bend). Highest turbulence levels in the proximal DAo were observed in aortas with significant flow separation from the inner arterial wall. Highest TKE levels in the AAO were seen in BV-1 which had a skewed and eccentric valvular flow and dilated AAO.

The next highest TKE levels are seen in BV-2 which had skewed and mildly eccentric valvular flow and a normal AAO diameter, followed by AV-Neo-1 which had a dilated AAO and a mildly eccentric jet. AV-Neo-2 had the smallest TKE levels which is unsurprising considering it has a central jet and AAO diameter within the healthy range. Elevations in turbulent WSS were correlated with near-wall regions of turbulence, meaning turbulent WSS was significant in all four aortas. When peak turbulent WSS values occur in the cardiac cycle, the contribution from turbulent WSS to total WSS ranges between 33.0% and 41.6% for all four aortas. Turbulent WSS exceeded laminar WSS for significant durations of the cardiac cycle. In the biological valves, turbulent WSS exceeds laminar WSS for 61.1% (BV-1) and 27.3% (BV-2) of the cardiac cycle. In AV-Neo valve types, turbulent WSS exceeds laminar WSS for 34.3% (AV-Neo-1) and 33.0% (AV-Neo-2) of the cardiac cycle. Turbulent WSS generally has the largest impact on total WSS during systolic deceleration and diastole.

Considering the small sample size, it is unclear which valve type performed best. However, this study sheds light into the mechanisms and complexity of turbulence production in the aorta. It is clear that an eccentric and skewed jet, and/or a dilated ascending aorta promote turbulence production in the ascending aorta. The findings of this study recommend that aortic valve treatments should prioritise minimising valvular eccentricity and skew in order to mitigate turbulence generation.

CRedit authorship contribution statement

Emily Louise Manchester: Conceptualization, Formal analysis, Investigation, Methodology, Visualization, Writing – original draft, Writing – review & editing. **Selene Pirola:** Methodology, Writing – review & editing. **Sergio Pirola:** Data curation, Writing – review & editing. **Giorgio Mastroiacovo:** Data curation, Writing – review & editing. **Gianluca Polvani:** Data curation, Writing – review & editing. **Gianluca Pontone:** Data curation, Writing – review & editing. **Xiao Yun Xu:** Conceptualization, Formal analysis, Writing – review & editing.

Declaration of competing interest

None declared.

Acknowledgements

EM was supported by a PhD scholarship through the EPSRC Doctoral Training Partnership grant to Imperial College London (EP/R512540/1). This work used the Cirrus UK National Tier-2 HPC Service at EPCC (<http://www.cirrus.ac.uk>) funded by the University of Edinburgh and EPSRC (EP/P020267/1).

Appendix A. Supplementary data

Supplementary material related to this article can be found online at <https://doi.org/10.1016/j.combiomed.2024.108123>.

References

- [1] P.R. Goody, M.R. Hosen, D. Christmann, S.T. Niepmann, A. Zietzer, M. Adam, F. Bönner, S. Zimmer, G. Nickenig, F. Jansen, Aortic valve stenosis: From basic mechanisms to novel therapeutic targets, *Arterioscl. Thrombosis Vasc. Biol.* 40 (2020) 885–900, <http://dx.doi.org/10.1161/ATVBAHA.119.313067>.
- [2] E. Minamino-Muta, T. Kato, T. Morimoto, T. Taniguchi, H. Shiomi, K. Nakatsuma, S. Shirai, K. Ando, N. Kanamori, K. Murata, T. Kitai, Y. Kawase, M. Miyake, C. Izumi, H. Mitsuoka, M. Kato, Y. Hirano, S. Matsuda, K. Nagao, T. Inada, T. Murakami, Y. Takeuchi, K. Yamane, M. Toyofuku, M. Ishii, M. Inoko, T. Ikeda, A. Komasa, E. Tada, K. Ishii, K. Hotta, N. Higashitani, T. Jinnai, Y. Kato, Y. Inuzuka, C. Maeda, Y. Morikami, N. Saito, R. Sakata, K. Minatoya, T. Kimura, Causes of death in patients with severe aortic stenosis: An observational study, *Sci. Rep.* 7 (2017) 14723, <http://dx.doi.org/10.1038/s41598-017-15316-6>.
- [3] R.A. Nishimura, Aortic valve disease, *Circulation* 106 (2002) 770–772, <http://dx.doi.org/10.1161/01.CIR.0000027621.26167.5E>.

- [4] M.D. Hope, T.A. Hope, S.E. Crook, K.G. Ordovas, T.H. Urbania, M.T. Alley, C.B. Higgins, 4D flow CMR in assessment of valve-related ascending aortic disease, *JACC: Cardiovasc. Imaging* 4 (2011) 781–787, <http://dx.doi.org/10.1016/j.jcmg.2011.05.004>.
- [5] E. Saliba, Y. Sia, The ascending aortic aneurysm: When to intervene? *IJC Heart Vasc.* 6 (2015) 91–100, <http://dx.doi.org/10.1016/j.ijcha.2015.01.009>.
- [6] Y. Agmon, B.K. Khandheria, I. Meissner, J.R.D. Sicks, W.M. O'Fallon, D.O. Wiebers, J.P. Whisnant, J.B. Seward, A.J. Tajik, Aortic valve sclerosis and aortic atherosclerosis: Different manifestations of the same disease? Insights from a population-based study, *J. Am. Coll. Cardiol.* 38 (2001) 827–834, [http://dx.doi.org/10.1016/S0735-1097\(01\)01422-X](http://dx.doi.org/10.1016/S0735-1097(01)01422-X).
- [7] S. Saeed, F. Scalise, J.B. Chambers, G. Mancina, Hypertension in aortic stenosis: A focused review and recommendations for clinical practice, *J. Hypertens.* 38 (2020) 1211–1219, <http://dx.doi.org/10.1097/HJH.0000000000002426>.
- [8] D.G. Guzzardi, A.J. Barker, P.V. Ooij, S.C. Malaisrie, J.J. Puthumana, D.D. Belke, H.E. Mewhort, D.A. Svystonyuk, S. Kang, S. Verma, J. Collins, J. Carr, R.O. Bonow, M. Markl, J.D. Thomas, P.M. McCarthy, P.W. Fedak, Valve-related hemodynamics mediate human bicuspid aortopathy: Insights from wall shear stress mapping, *J. Am. Coll. Cardiol.* 66 (2015) 892–900, <http://dx.doi.org/10.1016/j.jacc.2015.06.1310>.
- [9] F. Sotiropoulos, T.B. Le, A. Gilmanov, Fluid mechanics of heart valves and their replacements, *Annu. Rev. Fluid Mech.* 48 (2016) 259–283, <http://dx.doi.org/10.1146/annurev-fluid-122414-034314>.
- [10] A.B. Goldstone, P. Chiu, M. Baiocchi, B. Lingala, W.L. Patrick, M.P. Fischbein, Y.J. Woo, Mechanical or biologic prostheses for aortic-valve and mitral-valve replacement, *N. Engl. J. Med.* 377 (2017) 1847–1857, <http://dx.doi.org/10.1056/nejmoa1613792>.
- [11] S. Ozaki, I. Kawase, H. Yamashita, S. Uchida, Y. Nozawa, T. Matsuyama, M. Takatoh, S. Hagiwara, Aortic valve reconstruction using self-developed aortic valve plasty system in aortic valve disease, *Interact. CardioVasc. Thoracic Surg.* 12 (2011) 550–553, <http://dx.doi.org/10.1510/icvts.2010.253682>.
- [12] S. Ozaki, I. Kawase, H. Yamashita, S. Uchida, M. Takatoh, N. Kiyohara, Midterm outcomes after aortic valve neocuspidization with glutaraldehyde-treated autologous pericardium, *J. Thoracic Cardiovasc. Surg.* 155 (2018) 2379–2387, <http://dx.doi.org/10.1016/j.jtcvs.2018.01.087>.
- [13] S. Pirola, S. Pirola, G. Mastroiacovo, A. Bonomi, E.L. Manchester, S.M. Fischella, R. Maragna, A. Baggiano, S. Mushtaq, G. Muscogiuri, M. Guglielmo, X.Y. Xu, G. Pontone, G. Polvani, Does the AVNeo valve reduce wall stress on the aortic wall? A cardiac magnetic resonance analysis with 4D-flow for the evaluation of aortic valve replacement with the ozaki technique, *Eur. J. Cardio-Thoracic Surg.* (2023) <http://dx.doi.org/10.1093/ejcts/ezad299>.
- [14] A. Secinaro, E.G. Milano, P. Ciancarella, M. Trezzi, C. Capelli, P. Ciliberti, E. Cetrano, D. Curione, T.P. Santangelo, C. Napolitano, S.B. Albanese, A. Carotti, Blood flow characteristics after aortic valve neocuspidization in paediatric patients: A comparison with the ross procedure, *Eur. Heart J. - Cardiovasc. Imaging* 23 (2022) 275–282, <http://dx.doi.org/10.1093/ehjci/jeab009>.
- [15] H. Ha, M. Ziegler, M. Welander, N. Bjarnegård, C.J. Carlhäll, M. Lindenberger, T. Länne, T. Ebbens, P. Dyverfeldt, Age-related vascular changes affect turbulence in aortic blood flow, *Front. Physiol.* 9 (2018) 1–10, <http://dx.doi.org/10.3389/fphys.2018.00036>.
- [16] K.M. Saqr, S. Tupin, S. Rashad, T. Endo, K. Niizuma, T. Tominaga, M. Ohta, Physiologic blood flow is turbulent, *Sci. Rep.* 10 (2020) 15492, <http://dx.doi.org/10.1038/s41598-020-72309-8>.
- [17] E. Bollache, D.G. Guzzardi, S. Sattari, K.E. Olsen, E.S.D. Martino, S.C. Malaisrie, P. van Ooij, J. Collins, J. Carr, P.M. McCarthy, M. Markl, A.J. Barker, P.W. Fedak, Aortic valve-mediated wall shear stress is heterogeneous and predicts regional aortic elastic fiber thinning in bicuspid aortic valve-associated aortopathy, *J. Thoracic Cardiovasc. Surg.* 156 (2018) 2112–2120, <http://dx.doi.org/10.1016/j.jtcvs.2018.05.095>.
- [18] K.S. Cunningham, A.I. Gotlieb, The role of shear stress in the pathogenesis of atherosclerosis, *Lab. Invest.* 85 (2005) 9–23, <http://dx.doi.org/10.1038/labinvest.3700215>.
- [19] J.M. Dolan, J. Kolega, H. Meng, High Wall shear stress and spatial gradients in vascular pathology: A review, *Ann. Biomed. Eng.* 41 (2013) 1411–1427, <http://dx.doi.org/10.1038/jdci.10.1007/s10439-012-0695-0id.2014.371>.
- [20] C. Binter, A. Gotschy, S.H. Sündermann, M. Frank, F.C. Tanner, T.F. Lüscher, R. Manka, S. Kozerke, Turbulent kinetic energy assessed by multipoint 4-dimensional flow magn. res. imaging provides additional information relative to echocardiography for the determination of aortic stenosis severity, *Circul.: Cardiovasc. Imaging* 10 (2017) 1–8, <http://dx.doi.org/10.1161/CIRCIMAGING.116.005486>.
- [21] B. Becsek, L. Pietrasanta, D. Obrist, Turbulent systolic flow downstream of a bioprosthetic aortic valve: Velocity spectra, wall shear stresses, and turbulent dissipation rates, *Front. Physiol.* 11 (2020) 1–19, <http://dx.doi.org/10.3389/fphys.2020.577188>.
- [22] E.L. Manchester, S. Pirola, M.Y. Salmasi, D.P. O'Regan, T. Athanasiou, X.Y. Xu, Analysis of turbulence effects in a patient-specific aorta with aortic valve stenosis, *Cardiovasc. Eng. Technol.* 12 (2021) 438–453, <http://dx.doi.org/10.1007/s13239-021-00536-9>.
- [23] E.L. Manchester, S. Pirola, M.Y. Salmasi, D.P. O'Regan, T. Athanasiou, X.Y. Xu, Evaluation of computational methodologies for accurate prediction of wall shear stress and turbulence parameters in a patient-specific aorta, *Front. Bioeng. Biotechnol.* 10 (2022) 836611, <http://dx.doi.org/10.3389/fbioe.2022.836611>.
- [24] K.M. Saqr, K. Kano, S. Rashad, K. Niizuma, Y. Kaku, T. Iwama, T. Tominaga, Non-Kolmogorov turbulence in carotid artery stenosis and the impact of carotid stenting on near-wall turbulence, *AIP Adv.* 12 (2022) 015124, <http://dx.doi.org/10.1063/5.0076271>.
- [25] C. Vergara, D.L. Van, M. Quadrio, M. Domanin, Large eddy simulations of blood dynamics in abdominal aortic aneurysms, *Med. Eng. Phys.* 47 (2017) 38–46, <http://dx.doi.org/10.1016/j.medengphy.2017.06.030>.
- [26] P. Sagaut, Large Eddy Simulation for Incompressible Flows, third ed., Springer Berlin, 2006, <http://dx.doi.org/10.1007/B137536>.
- [27] U. Piomelli, Large-eddy simulation: Achievements and challenges, *Prog. Aerosp. Sci.* 35 (1999) 335–362, [http://dx.doi.org/10.1016/S0376-0421\(98\)00014-1](http://dx.doi.org/10.1016/S0376-0421(98)00014-1).
- [28] J. Lantz, T. Ebbens, J. Engvall, M. Karlsson, Numerical and experimental assessment of turbulent kinetic energy in an aortic coarctation, *J. Biomech.* 46 (2013) 1851–1858, <http://dx.doi.org/10.1016/j.jbiomech.2013.04.028>.
- [29] M. Andersson, J. Lantz, T. Ebbens, M. Karlsson, Multidirectional WSS disturbances in stenotic turbulent flows: A pre- and post-intervention study in an aortic coarctation, *J. Biomech.* 51 (2017) 8–16, <http://dx.doi.org/10.1016/j.jbiomech.2016.11.064>.
- [30] E.L. Manchester, X.Y. Xu, The effect of turbulence on transitional flow in the FDA's benchmark nozzle model using large-eddy simulation, *Int. J. Numer. Methods Biomed. Eng.* 36 (2020) 1–15, <http://dx.doi.org/10.1002/cnm.3389>.
- [31] S.B. Pope, Ten questions concerning the large-eddy simulation of turbulent flows, *New J. Phys.* 6 (2004) <http://dx.doi.org/10.1088/1367-2630/6/1/035>.
- [32] M.M. Mukaka, Statistics corner: A guide to appropriate use of correlation coefficient in medical research, *Malawi Med. J.* 24 (2012) 69–71.
- [33] T. Puiseux, A. Sewonu, O. Meyrignac, H. Rousseau, F. Nicoud, S. Mendez, R. Moreno, Reconciling PC-MRI and CFD: An in-vitro study, *NMR Biomed.* 32 (2019) 1–14, <http://dx.doi.org/10.1002/nbm.4063>.
- [34] P. Berg, D. Stucht, G. Janiga, O. Beuing, O. Speck, D. Thévenin, Cerebral blood flow in a healthy circle of willis and two intracranial aneurysms: Computational fluid dynamics versus four-dimensional phase-contrast magn. res. imaging, *J. Biomech. Eng.* 136 (2014) 1–9, <http://dx.doi.org/10.1115/1.4026108>.
- [35] A. Hager, H. Kaemmerer, U. Rapp-Bernhardt, S. Blücher, K. Rapp, T.M. Bernhardt, M. Galanski, J. Hess, Diameters of the thoracic aorta throughout life as measured with helical computed tomography, *J. Thoracic Cardiovasc. Surg.* 123 (2002) 1060–1066, <http://dx.doi.org/10.1067/jtc.2002.122310>.
- [36] P. Dyverfeldt, M.D. Hope, E.E. Tseng, D. Saloner, Magnetic resonance measurement of turbulent kinetic energy for the estimation of irreversible pressure loss in aortic stenosis, *JACC: Cardiovasc. Imaging* 6 (2013) 64–71, <http://dx.doi.org/10.1016/j.jcmg.2012.07.017>.
- [37] M. Andersson, M. Karlsson, Characterization of anisotropic turbulence behavior in pulsatile blood flow, *Biomech. Model. Mechanobiol.* 20 (2021) 491–506, <http://dx.doi.org/10.1007/s10237-020-01396-3>.
- [38] B. Alberts, A. Johnson, J. Lewis, M. Raff, K. Roberts, P. Walter, *Blood Vessels and Endothelial Cells*, fourth ed., Garland Science, New York, 2002, URL <https://www.ncbi.nlm.nih.gov/books/NBK26848/>.
- [39] J.J. Chiu, S. Chien, Effects of disturbed flow on vascular endothelium: Pathophysiological basis and clinical perspectives, *Physiol. Rev.* 91 (2011) 327–387, <http://dx.doi.org/10.1152/physrev.00047.2009>.
- [40] P.F. Davies, A. Remuzzi, E.J. Gordon, C.F.D. Jr, M.A.G. Jr, Turbulent fluid shear stress induces vascular endothelial cell turnover in vitro, *Proc. Natl. Acad. Sci. USA* 83 (1986) 2114–2117, <http://dx.doi.org/10.1073/pnas.83.7.2114>.
- [41] M. Kamenewa, G.W. Burgreen, K. Kono, B. Repko, J.F. Antaki, M. Umezu, Effects of turbulent stresses upon mechanical hemolysis: Experimental and computational analysis, *ASAIO J.* 50 (2004) 418–423, <http://dx.doi.org/10.1097/01.MAT.0000136512.36370.B5>.
- [42] H. Ha, J.P.E. Kvitting, P. Dyverfeldt, T. Ebbens, 4D flow MRI quantification of blood flow patterns, turbulence and pressure drop in normal and stenotic prosthetic heart valves, *Magn. Res. Imaging* 55 (2019) 118–127, <http://dx.doi.org/10.1016/j.mri.2018.09.024>.
- [43] J. Lantz, R. Gärdhagen, M. Karlsson, Quantifying turbulent wall shear stress in a subject specific human aorta using large eddy simulation, *Med. Eng. Phys.* 34 (2012) 1139–1148, <http://dx.doi.org/10.1016/j.medengphy.2011.12.002>.
- [44] M.Y. Salmasi, S. Pirola, S. Sasiidharan, S.M. Fischella, A. Redaelli, O.A. Jarral, D.P. O'Regan, A.Y. Oo, J.E. Moore, X.Y. Xu, T. Athanasiou, High wall shear stress can predict wall degradation in ascending aortic aneurysms: An integrated biomechanics study, *Front. Bioeng. Biotechnol.* 9 (2021) 935, <http://dx.doi.org/10.3389/fbioe.2021.750656>.
- [45] G. Soulat, M.B. Scott, B.D. Allen, R. Avery, R.O. Bonow, S.C. Malaisrie, P. McCarthy, P.W. Fedak, A.J. Barker, M. Markl, Association of regional wall shear stress and progressive ascending aorta dilation in bicuspid aortic valve, *JACC: Cardiovasc. Imaging* (2021) <http://dx.doi.org/10.1016/j.jcmg.2021.06.020>.
- [46] J.D. Humphrey, *Mechanisms of Vascular Remodeling in Hypertension*, vol. 34, Oxford University Press, 2021, pp. 432–441, <http://dx.doi.org/10.1093/ajh/hpaa195>.